Origin of enhanced water oxidation activity in an iridium single atom anchored on NiFe oxyhydroxide catalyst

Xueli Zheng[a,1], Jing Tang[a,b,1], Alessandro Gallo[c], Jose A. Garrido Torres[c], Xiaoyun Yu[a], Constantine J. Athanitis[a], Emily May Been[a], Peter Ercius[d], Haiyan Mao[e], Sirine C. Fakra[f], Chengyu Song[d], Ryan C. Davis[g], Jeffrey A. Reimer[e], John Vinson[h], Michal Bajdich[c,2], and Yi Cui[a,b,2]

[a]Department of Material Science and Engineering, Stanford University, Stanford, CA 94305; [b]Stanford Institute for Materials and Energy Sciences, SLAC National Accelerator Laboratory, Menlo Park, CA 94025; [c]SUNCAT Center for Interface Science and Catalysis, SLAC National Accelerator Laboratory, Menlo Park, CA 94025; [d]The Molecular Foundry, Lawrence Berkeley National Laboratory, Berkeley, CA 94720; [e]Department of Chemical and Biomolecular Engineering, University of California, Berkeley, CA 94720; [f]Advanced Light Source, Lawrence Berkeley National Laboratory, Berkeley, CA 94720; [g]Stanford Synchrotron Radiation Light Source, SLAC National Accelerator Laboratory, Menlo Park, CA 94025; and [h]Material Measurement Laboratory, National Institute of Standards and Technology, Gaithersburg, MD 20899

The efficiency of the synthesis of renewable fuels and feedstocks from electrical sources is limited, at present, by the sluggish water oxidation reaction. Single-atom catalysts (SACs) with a controllable coordination environment and exceptional atom utilization efficiency open new paradigms toward designing high-performance water oxidation catalysts. Here, using operando X-ray absorption spectroscopy measurements with calculations of spectra and electrochemical activity, we demonstrate that the origin of water oxidation activity of IrNiFe SACs is the presence of highly oxidized Ir single atom ($Ir^{5.3+}$) in the NiFe oxyhydroxide under operating conditions. We show that the optimal water oxidation catalyst could be achieved by systematically increasing the oxidation state and modulating the coordination environment of the Ir active sites anchored atop the NiFe oxyhydroxide layers. Based on the proposed mechanism, we have successfully anchored Ir single-atom sites on NiFe oxyhydroxides ($Ir_{0.1}/Ni_9Fe$ SAC) via a unique in situ cryogenic–photochemical reduction method that delivers an overpotential of 183 mV at $10\ mA \cdot cm^{-2}$ and retains its performance following 100 h of operation in 1 M KOH electrolyte, outperforming the reported catalysts and the commercial IrO_2 catalysts. These findings open the avenue toward an atomic-level understanding of the oxygen evolution of catalytic centers under in operando conditions.

highly oxidized Ir sites | water oxidation | operando X-ray absorption spectroscopy | DFT calculations

Efficient and cost-effective electrocatalysts play critical roles in energy conversion and storage and the societal pursuit of sustainable energy (1–3). The water oxidation reaction, also known as oxygen evolution reaction (OER), in particular, is an enabling process for diverse clean energy technologies, including water splitting (4–6), solar fuels (2), CO_2 reduction (7), and rechargeable metal–air batteries (8). Unfortunately, the kinetics of the OER are sluggish, which limits the power conversion efficiency and the overall efficiency.

Very recently, higher valence transition metal ions such as Co^{4+} (9–11), Ni^{4+} (12–14), and $Fe^{4+/5+}$ (15, 16) generated through a potential-dependent deprotonation reaction have been incorporated into metal oxides/hydroxides, resulting in enhanced water oxidation activity. Incorporating precious metals such as Ir, Ru, and Pt is much less explored, but they offer greater opportunities due to their tendency to form single-atom sites. Computational work has predicted either direct substitution of Ni^{4+} and Fe^{4+} by Ir^{4+} and Ru^{4+} or that the metal would be close to its most stable +4 oxidation state based on the high stability of the rutile phase (17–20). On the other hand, the high activity of Sr-leached $SrIrO_3/IrO_x$ and Li-removed Li_xIrO_3 catalysts

(5, 21, 22) and a recent prediction of highly active and high-oxidation homogeneous water oxidation systems (23) indicate that increased oxidation may lead to improved activity if the active site can be stabilized under operating conditions.

Single-atom catalysts (SACs) have offered an ideal system to precisely control the local coordination environments and oxidation states of the single-site centers (24–29). The single-atom nature of these active centers leads to well-defined coordination environments and enhanced metal–support interactions, which provide remarkable catalytic performance in a number of heterogeneous reactions, including in the water–gas shift reaction (24), heterogeneous reduction of CO_2 processes (27), CO oxidation (28), and oxygen reduction reaction (29). We adopted this strategy and sought to incorporate high-oxidation Ir metal sites into the support to enhance the water oxidation activity.

Here, we developed an in situ cryogenic–photochemical reduction method for anchoring Ir single sites on the NiFe oxyhydroxide support. Density functional theory (DFT) calculations predict unusually stable IrO_6 octahedral SAC anchored atop the

Significance

The efficiency with which renewable fuels and feedstocks are synthesized from electrical sources is largely limited by the sluggish water oxidation reaction. We show that the optimal water oxidation catalyst could be achieved by systematically modulating the coordination of the Ir active sites using an in situ cryogenic–photochemical reduction synthesis method. We achieved a highly oxidized Ir single site ($Ir^{+5.3}$) in the best atom utilization by single-atom catalysts on electrochemically stable supports. The origin of water oxidation activity in an Ir single-atom catalyst is revealed experimentally and theoretically. The concept and strategy of this work are expected to pioneer novel approaches to engineer single-atom catalysts.

ENGINEERING

NiFe oxyhydroxide layers. In operando Ir L_3-edge X-ray absorption spectroscopy (XAS) combined with spectra simulations of Ir L_3-edge of such structures revealed high oxidation of Ir (+5.3) in the NiFe oxyhydroxides under operating conditions, in agreement with DFT predictions and spectra calculations. The highly oxidized Ir single-site exhibits exceptional OER performance, with a 183 mV overpotential at 10 mA · cm^{-2}, outperforming the precious metal oxide IrO_2. These findings are further corroborated by our calculations of the theoretical OER overpotentials, which show that increasing the Ir oxidation state leads to improved activity, and an overpotential of 0.184 V is obtained for the most oxidized NiFeIr:3O SAC. Such structural and compositional heterogeneity poses a key obstacle to unambiguously identifying the exact atomistic structure of the active sites and to further establishing a definitive correlation with the catalytic properties that can guide the subsequent design of future generations of SACs.

Results and Discussion

Ir Single Sites on Ni_9Fe Oxyhydroxides. In order to test our hypothesis, we set out to explore how Ir is incorporated into NiFe oxyhydroxides. Using DFT, we have compared the free energy of Ir, substituting either Ni or Fe within the NiFeOOH layered structure (NiFe) to the free energy of anchoring oxidized Ir atop of the NiFe layer (Fig. 1A). For NiFe, we used a widely adopted γ-NiFeOOH bulk model with interlaced and solvated K^+ cations and protons since 1 M KOH was used as an electrolyte in the experiment (see *SI Appendix* for computational details) (18, 30, 31). Out of a large number of tested cases, only two possibilities had significant negative free energy of Ir doping (Fig. 1A and *SI Appendix*, Fig. S1). The two stable configurations are 1) a conventional in-layer substitutional doping of Ir^{4+} replacing Ni^{4+} (NiFeIr) (17, 18) and 2) single IrO_6 octahedron bonded directly to the NiFe layer, which we refer to as the SAC (NiFeIr SAC) configuration. A similar Ir–SAC configuration was recently proposed by Zhao et al. utilizing a Fe_2O_3 support (32). The protonation of the three outermost oxygens and the resulting Ir high-oxidation state in the NiFeIr SAC is a direct function of applied voltage (SAC NiFeIr:3OH versus NiFeIr:3O), but its stability is always greater than that of NiFeIr (>28 kJ/mol) (Fig. 1A and *SI Appendix*, Fig. S1). The remarkable ability of Ir to sustain a high-oxidation state, the availability to form multiple oxygen bonds at the NiFe layer, and the stabilization by nearby solvents allow for the presence of such a stable SAC configuration.

In light of the theoretical prediction, we sought to synthesize Ir single atoms on NiFe oxyhydroxides ($Ir_{0.1}/Ni_9Fe$ SAC) via the in situ cryogenic–photochemical reduction method (Fig. 1B). In this method, we first synthesized highly nanoporous Ni_9Fe oxyhydroxides as the support (6). Next, a mixed aqueous solution of $IrCl_3(H_2O)_3$ and Ni_9Fe oxyhydroxides was frozen quickly in liquid nitrogen (−196.5 °C) to form a thin layer of ice. Then, the frozen solution was exposed to ultraviolet (UV) irradiation on a cooling stage with a temperature of −35 °C for 1 h. After the UV treatment, the frozen solution was kept for 24 h in dark conditions at 4 °C. After centrifuging, washing, and freeze-drying the samples multiple times, the samples from the in situ cryogenic–photochemical process were stabilized on Ni_9Fe oxyhydroxide supports (*SI Appendix*). Aberration-corrected high-angle annular dark-field–scanning transmission electron microscopy (HAADF-STEM) showed Ir dispersed on Ni_9Fe oxyhydroxides as individual atoms (Fig. 1C). From inductively coupled plasma optical emission spectrometry (ICP-OES) analysis, the molar ratio of Ni:Fe:Ir to be 9:1:0.1 is determined. Clusters were formed when increasing the Ir loading on Ni_9FeOOH supports (*SI Appendix*, Fig. S2). Using the theoretical prediction and in situ cryogenic–photochemical synthesis, we have achieved stabilized and well-distributed Ir single-atom sites in the NiFe oxyhydroxides.

The Local Coordination and Electronic Structure of $Ir_{0.1}/Ni_9Fe$ SAC. To investigate the local electronic configuration and atomic structures of the $Ir_{0.1}/Ni_9Fe$ under OER operating conditions, we employed an in situ electrochemical cell for XAS measurements combined with absorption spectra simulations and extended X-ray absorption fine structure (EXAFS) fitting (Fig. 2). Electrochemistry was performed in a homemade cell using catalysts on carbon paper as a working electrode, an Ag/AgCl reference electrode, a platinum wire counter electrode, and 1 M KOH solution as the electrolyte (*SI Appendix*, Fig. S3).

The white lines (WLs) of Ir L_3-edge X-ray absorption near edge structure (XANES) spectra for NiFeIr SAC under different applied potentials were compared with the ones from standard Ir foil and commercial IrO_2 (Fig. 2A). For each condition, the Ir valence state was estimated from the position of the WL, which is expected to shift toward higher energy as the oxidation state increases. For $Ir_{0.1}/Ni_9Fe$ SAC at open circuit, the energy position of the WL is very close to that of IrO_2 reference, indicating a state close to Ir^{4+}. When the applied potential was raised to 1.35 V versus the reversible hydrogen electrode (RHE), the WL
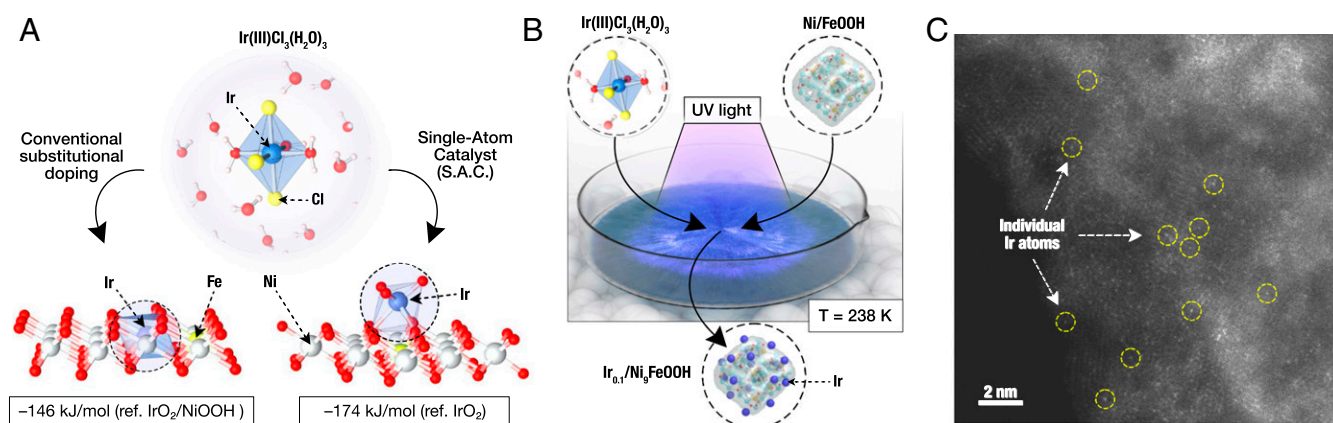
Fig. 1. The preparation route to Ir single-atom on NiFe oxyhydroxides and atomic structure characterizations of NiFeIr by HAADF-STEM. (*A*) A DFT prediction of a preferred Ir atom embedding within the NiFeOOH layered structure under operating conditions. The conventional in-layer substitution of Ni^{4+} by Ir^{4+} (NiFeIr) (*Left*) is compared to a more preferred single IrO_6 octahedron bonded to NiFe layer in SAC configuration (NiFeIr SAC) (*Right*). The energies with respect to given references are at zero bias. Note that NiFeIr SAC maintains its overall stability even under applied voltage (*SI Appendix*, Fig. S1). (*B*) In situ cryogenic–photochemical reduction synthesis of $Ir_{0.1}/Ni_9Fe$ samples. (*C*) HAADF-STEM image of Ir single atoms on Ni_9FeOOH supports ($Ir_{0.1}/Ni_9Fe$). Representative Ir single atoms are shown as bright spots with yellow circles.
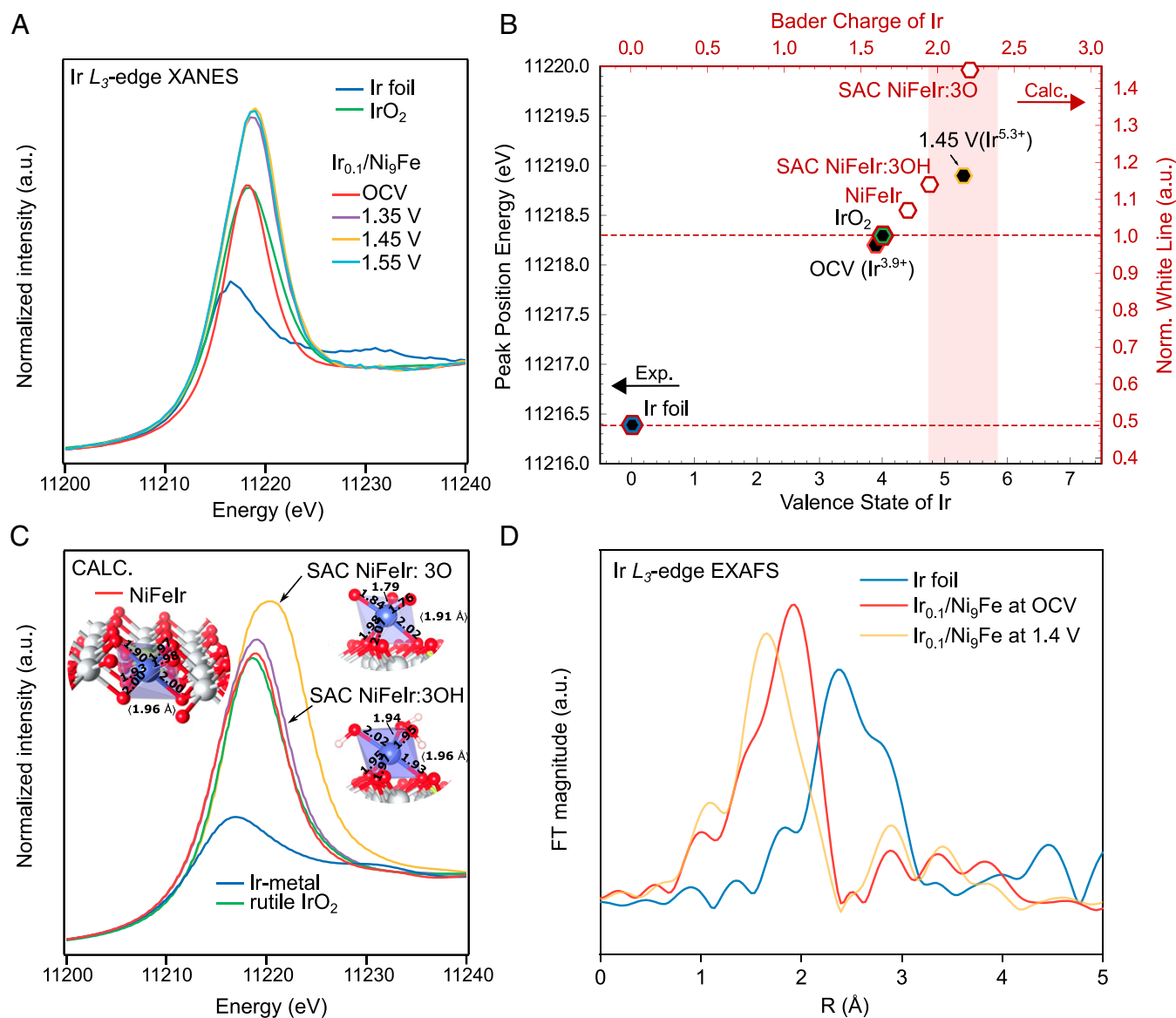
Fig. 2. In operando XAS characterization of the $Ir_{0.1}/Ni_9Fe$ catalyst coupled to DFT simulated spectra. (A) Experimental Ir-L_3 edge XANES spectra of $Ir_{0.1}/Ni_9Fe$ SAC at OCV and after applying 1.35 V, 1.45 V, and 1.55 V versus RHE. (B) WL position of $Ir_{0.1}/Ni_9Fe$ SAC during water oxidation reactions. Ir foil and IrO_2 were used as references for the oxidation states of 0 and +4. For comparison, the normalized WL intensity from DFT simulated spectra is also shown on the separate y-axis. Calculated Ir Bader charges indicating higher oxidation states for SAC structure are also shown on secondary x-axis. (C) Theoretical Ir L_3-edge XANES spectra of Ir foil, rutile-IrO_2, Ir doped sites (NiFeIr), and Ir anchored sites (NiFeIr SAC) (see also Figs. 1 and 4). Insets show the corresponding differences in the structural models. (D) Experimental Ir L_3-edge EXAFS spectra of Ir foil, $Ir_{0.1}/Ni_9Fe$ at OCV, and at 1.4 V versus RHE.

gradually shifted toward higher energies, in agreement with a prior study on the IrO_x/RuO_2 system (33). Using the WL position of Ir and IrO_2 as references and interpolating the rest of the samples to a linear dependency WL position versus valence (34), the XAS spectra indicated an Ir valence of +4 for $Ir_{0.1}/Ni_9Fe$ SAC at open circuit voltage (OCV) and +5.3 for $Ir_{0.1}/Ni_9Fe$ SAC at 1.45 V versus RHE, respectively (Fig. 2B). The position of the L_3 WL shifts toward higher energy and is in agreement with the expected electronic state: $5d^5$ (Ir^{4+}) for IrO_2 and $Ir_{0.1}/Ni_9Fe$ SAC at OCV and $5d^{3.7}$ ($Ir^{5.3+}$) for $Ir_{0.1}/Ni_9Fe$ SAC at 1.45 V versus RHE.

The OCEAN (Obtaining Core Excitations from Ab initio electronic structure and NIST core-level Bethe-Salpeter Equation) code (35, 36) simulation of the XANES region of the Ir L_3-edge (Fig. 2C; see also *SI Appendix* for details) on DFT-optimized structures introduced in Fig. 1A is in very good agreement with the

experimental data (Fig. 2A and *SI Appendix*, Fig. S4). The increase in the WL intensity from IrO_2 to the calculated NiFeIr SAC structures in the simulated data implies an increase in the oxidation state of the Ir atoms that well matches the experimental trend (Fig. 2C). This correlation is further supported when comparing the WL intensity of the calculated spectra versus DFT Bader charge (Fig. 2B). Particularly, the WL intensity obtained experimentally for $Ir_{0.1}/Ni_9Fe$ SAC under operating conditions is consistent with the simulated spectrum of NiFeIr:3OH SAC (Fig. 2C) and lies generally in between NiFeIr:3OH and NiFeIr:3O SAC (*SI Appendix*, Fig. S5), proving that Ir is present in the high-oxidation state under applied bias. Conversely, when the Ir atom substitutes one of the surface Ni atoms (NiFeIr), the Ir oxidation state is much closer to that of IrO_2 as evidenced by a peak height (Fig. 2C) and the decrease in WL intensity in the simulated spectrum (Fig. 2B). However, the maximum theoretical oxidation state is

not reached in the experiment, which is indicative of a possible mixture of the NiFeIr SAC and NiFeIr-type coordination in the $Ir_{0.1}/Ni_9Fe$ SAC sample. Judging from the DFT-calculated Bader charge results in optimized bulk structures, the electronic structures and charge of Ni and Fe atoms with and without Ir doping are very similar.

To further verify that $Ir_{0.1}/Ni_9Fe$ SAC contains only atomically dispersed individual Ir atoms, in situ EXAFS spectra were obtained for NiFeIr SAC at open circuit and at operating conditions (Fig. 2D). The Ir–Ir contribution at about 2.3 Å is absent in the k3-weighted EXAFS at the Ir L_3-edge for both NiFeIr SAC at open circuit and at 1.4 V versus RHE, strongly indicating that Ir exists as isolated atoms during operating conditions. The only prominent shell located in between 1.5 Å and 2 Å for $Ir_{0.1}/Ni_9Fe$ SAC at open circuit and at 1.4 V versus RHE, respectively, originated from the Ir-O contribution.

Evaluation of Water Oxidation Activity of $Ir_{0.1}/Ni_9Fe$ SAC. Next, we explored the water oxidation activity of $Ir_{0.1}/Ni_9Fe$ SAC and relevant controls on Ni foam in 1 M KOH electrolyte. The backward sweep was taken for the calculation of overpotential to avoid any nonfaradaic contribution to the total current. Although NiFe oxyhydroxides are indeed the best nonprecious metal electrocatalysts, further modification is needed to achieve better performance. The beneficial role of Au on NiFe LDH has been reported recently (37). The $Ir_{0.1}/Ni_9Fe$ SAC achieved the optimal water oxidation catalytic activity with the low overpotential of 183 mV at 10 mA · cm^{-2} (Fig. 3A), superior to that of the best commercial IrO_2 (~280 mV) (see also *SI Appendix*, Table S1 for detailed comparisons). The activity of $Ir_{0.1}/Ni_9Fe$ SAC is superior to that of the $Ir_{0.01}/Ni_9Fe$ owing to the formation of more Ir active sites (Fig. 3 A and B). However, upon incorporating higher Ir loading to 10%, the activity of Ir_1/Ni_9Fe catalyst decreased due to the formation of Ir clusters (*SI Appendix*, Fig. S2). The $Ir_{0.1}/Ni_9Fe$ SAC has the least Tafel

slope of 49 mV/dec, implying more favorable reaction kinetics toward water oxidation reaction than the control samples (38) (Fig. 3B). The electrochemical stability of the $Ir_{0.1}/Ni_9Fe$ SAC was tested at a constant overpotential of 200 mV on Ni foam for 100 h (Fig. 3C). We observed no appreciable decrease in current density in this time interval. We used HAADF-STEM characterizations to prove that no Ir–Ir bond was formed in the $Ir_{0.1}/Ni_9Fe$ SAC catalyst after electrochemical reaction, revealing the Ir atoms were dispersed at the atomic level (*SI Appendix*, Fig. S7). Obviously, the structure of Ir single sites after stability testing remained stable.

Lastly, we investigated whether the water oxidation activity of $Ir_{0.1}/Ni_9Fe$ SAC originates from intrinsic catalytic activity of Ir active sites or exclusively from an enhanced surface area. We analyzed the electrochemically active surface area (ECSA) and ECSA-normalized current density at 1.45 V versus RHE for $Ir_{0.1}/Ni_9Fe$ SAC and Ni_9FeOOH control (Fig. 3D). Based on ECSA results, the intrinsic activity of $Ir_{0.1}/Ni_9Fe$ SAC is higher than that of Ni_9FeOOH control. $Ir_{0.1}/Ni_9Fe$ SAC shows the advantages not only in improving OER activity and stability but also lowering Ir usage and cost.

Theoretical Activities of NiFeIr Water Oxidation Catalysts. To complete our analysis of $Ir_{0.1}/Ni_9Fe$ SAC system, we evaluated theoretical OER overpotentials (*SI Appendix, Computational Details*) of the obtained stable systems using Ir at edge sites, subsurface, and as single-atom near Fe sites [adapted from an Au single-atom study (37)] in the (100) surface of NiFe labeled as NiFeIr and octahedral NiFeIr SAC anchored at the NiFe basal planes [(001) facet]. These are compared to the (110) surface of rutile IrO_2 and to the Fe site in NiFe (100) surface obtained previously (31). First, we show that the calculated ΔG_{OOH} to ΔG_{OH} scaling (Fig. 4A) for Ir sites is generally improved over the universal scaling, where OOH* is stabilized with nearby surface oxygens, and is also necessary in order to obtain theoretical overpotentials lower than 0.3
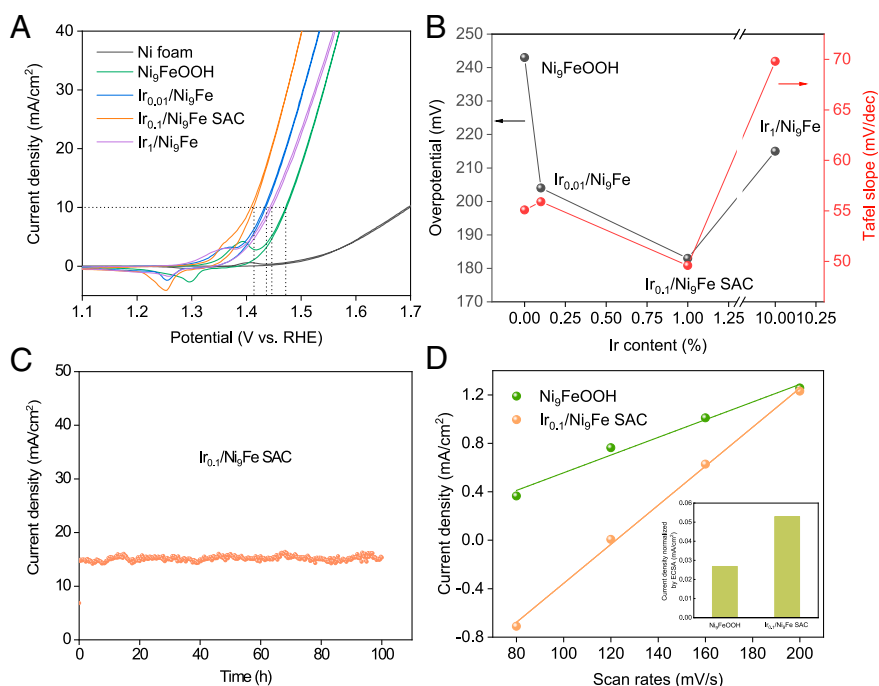
Fig. 3. Performance of $Ir_{0.1}/Ni_9Fe$ SAC and controls in the three-electrode system. (*A*) The OER polarization curves and (*B*) overpotential at 10 mA · cm^{-2} and Tafel slopes of $Ir_{0.1}/Ni_9Fe$ SAC and controls loaded on Ni foam in 1 M KOH. (*C*) Chronoamperometry measurement of $Ir_{0.1}/Ni_9Fe$ SAC on Ni foam electrode at a constant potential of 1.43 V versus RHE for 100 h. (*D*) Current density of $Ir_{0.1}/Ni_9Fe$ SAC and Ni_9FeOOH control plotted versus scan rates. The slopes obtained from a linear fit were used to represent ECSA. The inset shows the ECSA normalized current density at 1.45 V versus RHE for $Ir_{0.1}/Ni_9Fe$ SAC and Ni_9FeOOH, respectively.

V. Additionally, the sites with Ir in higher oxidation states bind the adsorbates progressively, which further increases the OOH* stabilization. Theoretically, adding Ir into NiFe oxyhydroxides significantly improves the second step (OH* to O*) in the OER mechanism for Ir sites (Fig. 4B and *SI Appendix*, Fig. S9). The theoretical OER overpotentials, shown as a two-dimensional (2D) OER volcano plot, are summarized in Fig. 4B.

The 2D volcano plot further shows that the Ir site in the IrO$_2$(110) binds significantly stronger (ΔG_{OH} is the most negative in Fig. 4 A and B) than any other model considered and appears in the lower-left part of the 2D plot. On the other hand, the Fe site in the NiFe (100) binds significantly weaker due to the presence the Fe-O oxo intermediate (ΔG_{OH} is the most positive in Fig. 4 A and B) and appears in the upper-right part of the 2D plot. Additionally, we have tested the effect captured by Zhang et al. for Au/NiFe LDHs on Fe sites (37). Our expanded calculations (*SI Appendix*, Fig. S9) show that the effect of adding Ir is different than that of adding Au in Ni$_9$FeOOH. Adding single-atom Ir next to the Fe-active site [*SI Appendix*, Fig. S9, structure (i)] results in very reactive O* at the Ir-O-Fe bridge, which leads to unfavorable O* to OOH* OER step with overpotential of 1.8 V. For completeness, we have also tested the effect of subsurface doping by Ir next to the Fe-active site [*SI Appendix*, Fig. S9, structure (h)]. In all tested cases, adding Ir next to Fe did not improve the activity of the Fe-active site, indicating no synergetic interaction of Ir on Fe sites in the NiFe oxyhydroxides. Interestingly, all Ir sites in the NiFeIr and NiFeIr SAC models straddled two extrema set by two structures (Fig. 4 D and E) in a nearly linear fashion. This trend is well-correlated with the formal and calculated oxidation states of the Ir sites in the NiFeIr (+4.4) and NiFeIr SAC (+4.8 and +5.6) models (Fig. 2B). Improved OH-OOH scaling and a gradual decrease of 5d electrons at the Ir atoms to bond with active oxygen 2p states—indicative of weaker adsorbate bonding—in turn shifts the position of the NiFeIr SAC model inside the optimal OER region. A similar system on Ir-anchored NiFe oxyhydroxides was developed, in which they discovered that the isolated Ir sites undergo a deprotonation process to form the multiple Ir$^{+3.57}$ active sites during OER, promoting the O–O coupling (39). The final calculated theoretical overpotentials are 0.184 V for NiFeIr:3O SAC (Fig. 4G), 0.333 V for the Ir site in NiFeIr(100) (Fig. 4F), 0.381 V for the Fe site in NiFe(100) (Fig. 4E), and, finally, 0.664 V for IrO$_2$ (110) (Fig. 4D). The very low overpotential of 0.184 V for NiFeIr SAC is obtained only for well-stabilized OOH intermediates and agrees well with the experimental overpotential of 183 mV for Ir$_{0.1}$/Ni$_9$Fe SAC catalyst. A detailed list of DFT energies and structures is provided via the catalysis-hub.org repository (40, 41).

Conclusions

In summary, we established a protocol in which Ir single-atom sites are stabilized on NiFe oxyhydroxides via an in situ cryogenic–photochemical reduction method, which leads to Ir$_{0.1}$/Ni$_9$Fe SAC catalysts with superior water oxidation performance. By combining XAS analyses with simulated spectra and calculated OER activity, we unambiguously identify that Ir species adopt a single-atom configuration in an oxidation state greater than +5. The Ir$_{0.1}$/Ni$_9$Fe SAC delivers an overpotential of 183 mV at 10 mA · cm^{-2}, which halves the 0.3 to 0.4 V OER
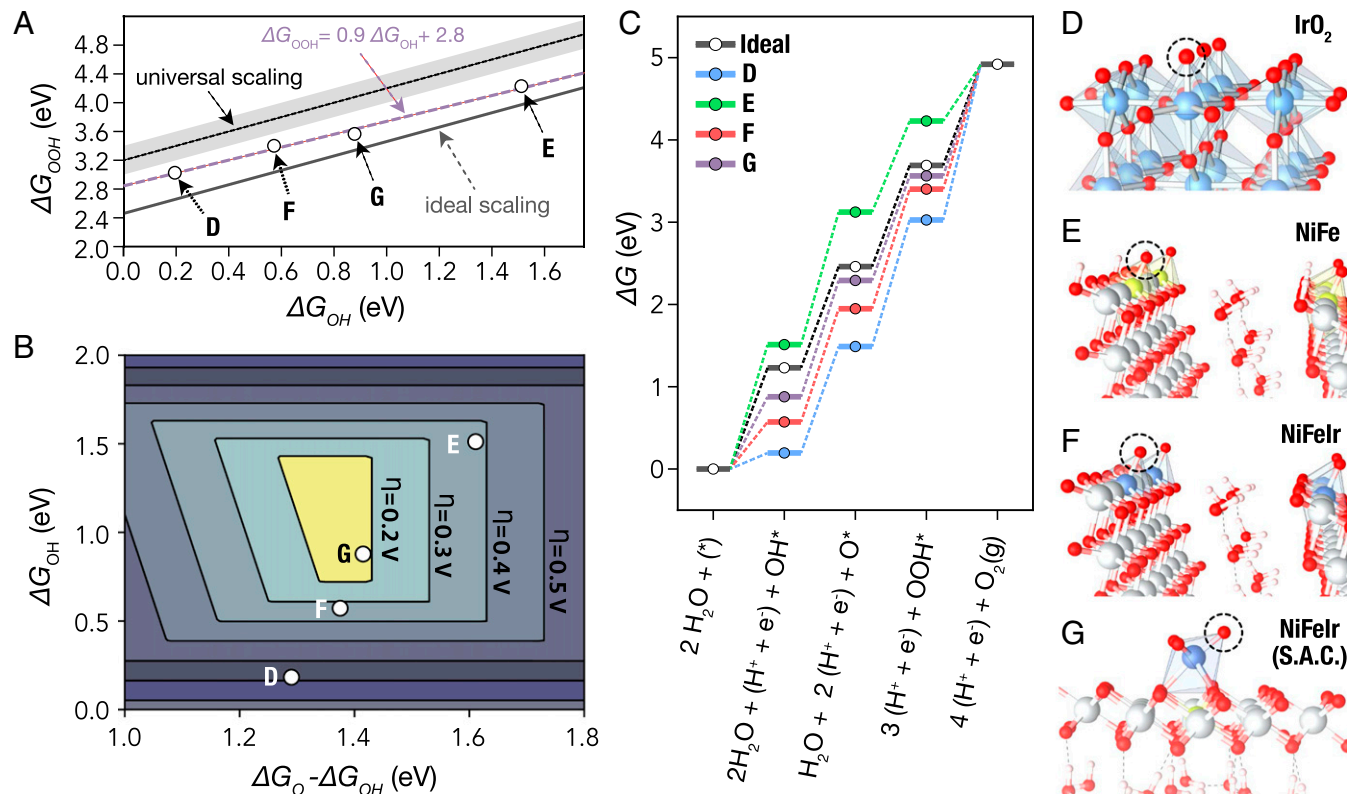
Fig. 4. Tuning the OER energetics of NiFeOOH via Ir site engineering. (*A*) Improved ΔG_{OOH} to ΔG_{OH} (OH-OOH) scaling ($\Delta G_{OOH} = \Delta G_{OH} + 2.686$ eV) for the *D–G* models relative to the universal and ideal scaling lines. (*B*) Two-dimensional activity volcano plot with optimal region (shown in yellow) based on the (*A*) scaling and with positions of the thermodynamis for *D–G* systems. (*C*) Free energy diagram of the OER mechanism of our models relative to ideal catalyst (at U = 0 V), highlighting the close similarity with model *G*. (*D–G*) Structural models: (*D*) (110) surface of rutile-IrO$_2$ (IrO$_2$), (*E*) (100) surface of NiFe, (*F*) Ir site in the (100) surface of NiFeIr, and (*G*) (001) basal plane of NiFeIr SAC. Results for additional tested structures are shown in *SI Appendix*, Fig. S8. All structures are shown with the O* as adsorption intermediate. The atom colors are Ir, light blue; Fe, yellow; Ni, light gray; O, red; and H, light pink.

Zheng et al.
Origin of enhanced water oxidation activity in an iridium single atom anchored on NiFe oxyhydroxide catalyst

PNAS | 5 of 7
https://doi.org/10.1073/pnas.2101817118

overpotential wall and is superior to most Ir-based catalysts known to date. The above experimental findings are further corroborated by the DFT calculations, which show that the improved activity is due to weaker binding and improved OH-OOH scaling of the highly oxidized Ir–SAC sites. Importantly, the utilization of NiFe oxyhydroxides as catalytic support provides an ideal model system to probe and quantitatively establish the correlation between the atomistic structure of the single-metal centers and their catalytic properties for a diverse set of electrocatalytic reactions. Our findings demonstrate unique electrochemical properties of SACs, with general implications for the design of materials employing oxygen redox chemistry.

Materials and Methods

Preparation of Ir Single Atoms/NiFe. Our general in situ cryogenic–photochemical reduction synthesis of Ir single atoms/Ni$_9$FeOOH is illustrated in Fig. 1B. First, a controlled ratio of 0.1 mg · mL^{-1} IrCl$_3$(H$_2$O)$_3$ and Ni$_9$FeOOH in aqueous solution was prepared in a beaker, and the beaker was frozen quickly in a liquid nitrogen (−196.5 °C) bath in dark conditions, keeping the beaker flat. The mixed solution can be frozen quickly to form ultrathin ice, which ensures that the homogeneous distribution of Ir precursor molecules in the solution can be maintained during the solidification process. Second, the frozen ice was exposed to UV irradiation on a cooling stage with a temperature of −35 °C for 1 h in an environmental chamber (Associated Environmental Systems), avoiding ice melting and forming Ir single atoms on Ni$_9$FeOOH support. The powder density of the UV light near ice was measured (0.7 mW · cm^{-2}) using a radiometer (Newport Model PMKIT-05-01). Then, the Ir single atoms on Ni$_9$FeOOH samples were filtered, cleaned, and dried in vacuo in a Labconco FreeZone 6 freeze dryer. Finally, the Ir$_{0.1}$/Ni$_9$Fe SACs were collected.

Characterization. HAADF-STEM was taken on a TEAM 0.5 transmission electron microscope operated at 300 kV at the National Center for Electron Microscopy. The samples were prepared by dropping catalyst powder dispersed in ethanol onto carbon-coated copper TEM grids (Ted Pella) using micropipettes and were dried under ambient conditions. The atomic composition of Ir/NiFe catalyst was determined using an ICP-OES (Agilent 720 with a hermetically sealed charge-coupled device (CCD) detector).

In Situ X-ray Absorption. In the homemade cell, electrochemistry was performed using catalysts on carbon paper as a working electrode, an Ag/AgCl reference electrode, a platinum wire counter electrode, and 1 M KOH solution as the electrolyte (*SI Appendix*, Fig. S3). The in situ Ir L$_3$-edge XAS data were collected at the X-Ray Fluorescence Microprobe beamline 10.3.2 of the Advanced Light Source (ALS) and beamline 4-1 at the Stanford Synchrotron Radiation Lightsource. The ALS data were preprocessed (deadtime corrected, calibrated, and deglitched) using custom LabVIEW software available at the beamline. The spectra were further aligned, calibrated, and normalized using Athena software (Demeter version 0.9.26). To extract EXAFS oscillations, the background was removed in k-space using a five-domain cubic spline. Ir L$_3$-edge EXAFS were fitted in R-space using artemis with the DFT-optimized NiFeIr:3Os model (*SI Appendix*, Fig. S8).

Electrochemical Measurements. Electrochemical measurements were performed using a three-electrode system connected to an electrochemical workstation (Bio-Logic VMP3) with a built-in electrochemical impedance spectroscopy analyzer. The working electrode was catalysts deposited on Ni foam. Ag/AgCl (with saturated KCl as the filling solution) and platinum foil were used as reference and counter electrodes, respectively. To load the catalyst on a Ni foam, 20 mg of catalyst was dispersed in a mixture containing 2 mL of water and 2 mL ethanol, followed by the addition of 100 μL Nafion solution. The suspension was sonicated for 30 min to prepare a homogeneous ink. Ni foam coated with water-resistant silicone glue was drop-casted with the catalyst ink. Unless otherwise stated, all experiments were performed at ambient temperature (22 ± 2 °C). Electrode potentials were converted to the RHE based on the following equation: E(RHE) = E(Ag/AgCl) + 0.197 V + 0.059 × pH.

The ECSA of each catalyst was calculated based on measuring their electrochemical capacitances. We measured the CVs in a narrow non-Faradaic potential window in which the change of the current is principally due to the charging of the double-layer, which is expected to be linearly proportional to the active surface area. The measured capacitive current densities at the average potential in the selected range were plotted as a function of

scan rates. The slope of the linear fit was calculated as the double-layer capacitance (C$_{dl}$). The ECSA of the catalyst is calculated from the following equation:

$$ECSA = \frac{C_{dl}}{C_s}cm^2_{ECSA} \quad ECSA = C_{dl}/C_s.$$

C$_s$ is the specific capacitance in 1 M KOH electrolyte. The intrinsic activity was obtained by normalizing the current to the ECSA to exclude the effect of surface area on catalytic performance.

DFT Calculations of Bulk and Surface Models. The density functional calculations were performed within the Vienna ab initio simulation package using the projector-augmented wave potentials. We employed the Perdew-Burke-Ernzerh (PBE) functional together with the Hubbard-U correction method applied for the d-electrons of Ni (U-J = U$_{eff}$ = 6.45 eV) and Fe (U$_{eff}$ = 4.3 eV) atoms. For Ni, the U$_{eff}$ parameter was chosen according to the Materials Project Database, while for Fe, it was taken from recent NiFeOOH paper of Martirez and Carter (42). For NiFeOOH system, other authors have used similar values for NiFeOOH that are within +/−1 eV. The bulk optimization calculations were performed at the energy cutoff of 600 eV on the 3 × 3 × 4 k-point mesh per 3 × 3 × 2 unit cell of the NiFeOOH [K$_8$(Ni$_{22}$Fe$_2$)O$_{48}$ + 16H$_2$O] used in our recent work. In this cell, a single Ir atom was placed either in the conventional in-layer substitutional doping (replacing Ni^{4+}, Ni^{3+}, and Fe^{4+} sites) or in the SAC configuration relative to Ni and Fe and variable OH*/O* groups (see results in *SI Appendix*, Fig. S1).

For surfaces, we have employed 3 × 1 symmetric (100) slabs of four layers of M–O (keeping the bottom two fixed) and 3 × 2 × 2 (001) basal plane (bottom layer fixed) and 15 Å of a vacuum. Here, we used 500 eV energy cutoff and the 4 × 4 × 1 and (3 × 3 × 1) k-point meshes, respectively. Full relaxation below a minimum threshold force of 0.02 eV/Å^2 was performed in all cases. To obtain the theoretical overpotential for each surface, the standard OER mechanism and which has been applied to many types of oxides [* → OH*, OH* → O*, O* → OOH*, OOH* → O$_2$(g)] was assumed. The Gibbs free energies of the OER intermediates calculated via the computational hydrogen electrode method include room temperature corrections, zero-point energy, and the vibrational enthalpy and entropy contributions [relative to H$_2$(g) and H$_2$O(l)] obtained by means of the harmonic approximation. The combined effect of total energies of adsorption is ΔG$_{corr.}$(OH*) = 0.302 eV, ΔG$_{corr.}$(O*) = −0.015 eV, and ΔG$_{corr.}$(OOH*) = 0.345 eV, respectively. The fully optimized bulk models, reference structures, and their respective energies are included as part of the catalysis-hub.org repository.

Computation of the Spectra. The Ir L$_3$-edge for the different structures was calculated using the OCEAN code. Electron wave functions were generated using the QUANTUMESPRESSO code. The norm-conserving pseudopotentials for Ir and O generated using the FHI98PP package using Trouiller–Martins type, PBE-generalized gradient approximation (GGA) was utilized. For the simulation of rutile IrO$_2$ and Ir metal, experimental crystallographic structures were used (Inorganic Crystal Structure Database [ICSD] #84577 and #640730, respectively) with a k-points sampling of (4 × 4 × 4), 1,000 screening bands, and (2 × 2 × 2) k-points sampling for the screening calculation. For the DFT generated structures, the k-points sampling was decreased to (2 × 2 × 1) with 2,000 screening bands. The same core-offset energy, plane-wave energy cutoff (120 Rydberg), and broadening (3.5 eV) were utilized for all the simulations.

The simulated spectra were normalized and aligned to the experimental results. The WL was numerically integrated after fitting the data using Lorentzian and arctangent fit function (*SI Appendix*, Fig. S4). The WL intensity was normalized by the WL intensity of the simulation for rutile IrO$_2$. The WLs of the experimental data were normalized in the same way using the experimental IrO$_2$ as standard.

6 of 7 | PNAS
https://doi.org/10.1073/pnas.2101817118

Zheng et al.
Origin of enhanced water oxidation activity in an iridium single atom anchored on NiFe oxyhydroxide catalyst

1. P. De Luna et al., What would it take for renewably powered electrosynthesis to displace petrochemical processes? Science 364, eaav3506 (2019).
2. H. B. Gray, Powering the planet with solar fuel. Nat. Chem. 1, 7 (2009).
3. Z. W. Seh et al., Combining theory and experiment in electrocatalysis: Insights into materials design. Science 355, eaad4998 (2017).
4. T. Wu et al., Iron-facilitated dynamic active-site generation on spinel $CoAl_2O_4$ with self-termination of surface reconstruction for water oxidation. Nat. Catal. 2, 763–772 (2019).
5. L. C. Seitz et al., A highly active and stable $IrO_x/SrIrO_3$ catalyst for the oxygen evolution reaction. Science 353, 1011–1014 (2016).
6. B. Zhang et al., Homogeneously dispersed multimetal oxygen-evolving catalysts. Science 352, 333–337 (2016).
7. X. Zheng et al., Theory-driven design of high-valence metal sites for water oxidation confirmed using in situ soft X-ray absorption. Nat. Chem. 10, 149–154 (2018).
8. P. Albertus, S. Babinec, S. Litzelman, A. Newman, Status and challenges in enabling the lithium metal electrode for high-energy and low-cost rechargeable batteries. Nat. Energy 3, 16–21 (2017).
9. J. Zhou et al., Electrochemically accessing ultrathin Co (oxy)-hydroxide nanosheets and operando identifying their active phase for the oxygen evolution reaction. Energy Environ. Sci. 12, 739–746 (2019).
10. A. Moysiadou, S. Lee, C. S. Hsu, H. M. Chen, X. Hu, Mechanism of oxygen evolution catalyzed by cobalt oxyhydroxide: Cobalt superoxide species as a key intermediate and dioxygen release as a rate-determining step. J. Am. Chem. Soc. 142, 11901–11914 (2020).
11. M. Bajdich, M. García-Mota, A. Vojvodic, J. K. Nørskov, A. T. Bell, Theoretical investigation of the activity of cobalt oxides for the electrochemical oxidation of water. J. Am. Chem. Soc. 135, 13521–13530 (2013).
12. X. Su et al., Operando spectroscopic identification of active sites in NiFe prussian blue analogues as electrocatalysts: Activation of oxygen atoms for oxygen evolution reaction. J. Am. Chem. Soc. 140, 11286–11292 (2018).
13. M. Görlin et al., Oxygen evolution reaction dynamics, faradaic charge efficiency, and the active metal redox states of Ni-Fe oxide water splitting electrocatalysts. J. Am. Chem. Soc. 138, 5603–5614 (2016).
14. D. K. Bediako et al., Structure-activity correlations in a nickel-borate oxygen evolution catalyst. J. Am. Chem. Soc. 134, 6801–6809 (2012).
15. J. Y. Chen et al., Operando analysis of NiFe and Fe oxyhydroxide electrocatalysts for water oxidation: Detection of Fe^{4+} by Mössbauer spectroscopy. J. Am. Chem. Soc. 137, 15090–15093 (2015).
16. H. Dau, Water splitting: Unexpected Fe(VI) trapped by manipulation of reaction kinetics. Chem 4, 668–670 (2018).
17. V. Tripkovic, H. A. Hansen, T. Vegge, From 3D to 2D Co and Ni oxyhydroxide catalysts: Elucidation of the active site and influence of doping on the oxygen evolution activity. ACS Catal. 7, 8558–8571 (2017).
18. H. Shin, H. Xiao, W. A. Goddard 3rd, In silico discovery of new dopants for Fe-doped Ni oxyhydroxide ($Ni_{1-x}Fe_xOOH$) catalysts for oxygen evolution reaction. J. Am. Chem. Soc. 140, 6745–6748 (2018).
19. P. Li et al., Boosting oxygen evolution of single-atomic ruthenium through electronic coupling with cobalt-iron layered double hydroxides. Nat. Commun. 10, 1711 (2019).
20. H. N. Nong et al., A unique oxygen ligand environment facilitates water oxidation in hole-doped $IrNiO_x$ core–shell electrocatalysts. Nat. Catal. 1, 841–851 (2018).
21. P. E. Pearce et al., Revealing the reactivity of the iridium trioxide intermediate for the oxygen evolution reaction in acidic media. Chem. Mater. 31, 5845–5855 (2019).
22. C. Yang et al., Cation insertion to break the activity/stability relationship for highly active oxygen evolution reaction catalyst. Nat. Commun. 11, 1378 (2020).
23. M. J. Craig et al., Universal scaling relations for the rational design of molecular water oxidation catalysts with near-zero overpotential. Nat. Commun. 10, 4993 (2019).
24. S. Yao et al., Atomic-layered Au clusters on α-MoC as catalysts for the low-temperature water-gas shift reaction. Science 357, 389–393 (2017).
25. Y. Yao et al., High temperature shockwave stabilized single atoms. Nat. Nanotechnol. 14, 851–857 (2019).
26. H. Wei et al., Iced photochemical reduction to synthesize atomically dispersed metals by suppressing nanocrystal growth. Nat. Commun. 8, 1490 (2017).
27. X. Shao et al., Iridium single-atom catalyst performing a Quasi-homogeneous hydrogenation transformation of CO_2 to formate. Chem 5, 693–705 (2019).
28. Y. Lu et al., Identification of the active complex for CO oxidation over single-atom Ir-on-$MgAl_2O_4$ catalysts. Nat. Catal. 2, 149–156 (2018).
29. H. Fei et al., General synthesis and definitive structural identification of MN_4C_4 single-atom catalysts with tunable electrocatalytic activities. Nat. Catal. 1, 63–72 (2018).
30. J. Zaffran et al., Influence of electrolyte cations on Ni(Fe)OOH catalyzed oxygen evolution reaction. Chem. Mater. 29, 4761–4767 (2017).
31. J. G. Baker et al., The role of aluminum in promoting Ni–Fe–OOH electrocatalysts for the oxygen evolution reaction. ACS Appl. Energy Mater. 2, 3488–3499 (2019).
32. Y. Zhao et al., Stable iridium dinuclear heterogeneous catalysts supported on metal-oxide substrate for solar water oxidation. Proc. Natl. Acad. Sci. U.S.A. 115, 2902–2907 (2018).
33. A. F. Pedersen et al., Operando XAS study of the surface oxidation state on a monolayer IrO_x on RuO_x and Ru oxide based nanoparticles for oxygen evolution in acidic media. J. Phys. Chem. B 122, 878–887 (2018).
34. J. P. Clancy et al., Spin-orbit coupling in iridium-based 5d compounds probed by x-ray absorption spectroscopy. Phys. Rev. B 86, 195131 (2012).
35. J. Vinson, J. J. Rehr, J. J. Kas, E. L. Shirley, Bethe-Salpeter equation calculations of core excitation spectra. Phys. Rev. B Condens. Matter Mater. Phys. 83 (2011).
36. K. Gilmore et al., Efficient implementation of core-excitation Bethe–Salpeter equation calculations. Comput. Phys. Commun. 197, 109–117 (2015).
37. J. Zhang et al., Single-atom Au/NiFe layered double hydroxide electrocatalyst: Probing the origin of activity for oxygen evolution reaction. J. Am. Chem. Soc. 140, 3876–3879 (2018).
38. Y.-H. Fang, Z.-P. Liu, Tafel kinetics of electrocatalytic reactions: From experiment to first-principles. ACS Catal. 4, 4364–4376 (2014).
39. K. Jiang et al., Dynamic active-site generation of atomic iridium stabilized on nanoporous metal phosphides for water oxidation. Nat. Commun. 11, 2701 (2020).
40. K. T. Winther et al., Catalysis-Hub.org, an open electronic structure database for surface reactions. Sci. Data 6, 75 (2019).
41. X. Zheng et al., Online Computational Data. https://www.catalysis-hub.org/publications/ZhengOrigin2020. Accessed 18 August 2021.
42. J. M. P. Martirez, E. A. Carter, Unraveling oxygen evolution on iron-doped beta-nickel oxyhydroxide: The key role of highly active molecular-like sites. J. Am. Chem. Soc. 141, 693–705 (2019).

ENGINEERING

Zheng et al.
Origin of enhanced water oxidation activity in an iridium single atom anchored on NiFe oxyhydroxide catalyst

PNAS | 7 of 7
https://doi.org/10.1073/pnas.2101817118